Geophysical Research Letters

RESEARCH LETTER
10.1029/2021GL092692

Deriving Melt Rates at a Complex Ice Shelf Base Using In Situ Radar: Application to Totten Ice Shelf

Irena Vaňková[1], Sue Cook[2], J. Paul Winberry[3], Keith W. Nicholls[1], and Benjamin K. Galton-Fenzi[2,4]

[1]British Antarctic Survey, Natural Environment Research Council, Cambridge, UK, [2]Australian Antarctic Program Partnership, Institute for Marine and Antarctic Studies, University of Tasmania, Hobart, TAS, Australia, [3]Department of Geological Sciences, Central Washington University, Ellensburg, WA, USA, [4]Australian Antarctic Division, Kingston, TAS, Australia

Key Points:

- First in situ radar-derived basal melt estimate on Totten Ice Shelf yields 22 ± 2.1 m a^{-1}, at least 40% lower than existing satellite estimates
- Radar-derived observation of tidal ice dynamics constrains estimate of ice thickness for a complex base
- The use of multiple basal reflections in melt derivation increases robustness of the estimate when early off-nadir returns are present

Supporting Information:

Supporting Information may be found in the online version of this article.

Correspondence to:

I. Vaňková,
irkova@bas.ac.uk

Citation:

Vaňková, I., Cook, S., Winberry, J. P., Nicholls, K. W., & Galton-Fenzi, B. K. (2021). Deriving melt rates at a complex ice shelf base using in situ radar: Application to Totten Ice Shelf. *Geophysical Research Letters*, *48*, e2021GL092692. https://doi.org/10.1029/2021GL092692

Received 25 JAN 2021
Accepted 18 FEB 2021

Abstract A phase-sensitive radar (ApRES) was deployed on Totten Ice Shelf to provide the first in situ basal melt estimate at this dynamic East Antarctic ice shelf. Observations of internal ice dynamics at tidal time scales showed that early arrivals from off-nadir reflectors obscure the true depth of the ice shelf base. Using the observed tidal deformation, the true base was found to lie at 1,910–1,950-m depth, at 350–400 m greater range than the first reflection from an ice-ocean interface. The robustness of the basal melt rate estimate was increased by using multiple basal reflections over the radar footprint, yielding a melt rate of 22 ± 2.1 m a^{-1}. The ApRES estimate is over 40% lower than the three existing satellite estimates covering Totten Ice Shelf. This difference in basal melt is dynamically significant and highlights the need for independent melt rate estimates using complementary instrumentation and techniques that rely on different sets of assumptions.

Plain Language Summary Observations of the rate of melting at the base of ice shelves are needed to model accurately ice sheet evolution. Local measurements are scarce, yet necessary for validation of satellite products and ocean models. We deployed a phase-sensitive radar in the proximity of grounding zone of Totten Ice Shelf in East Antarctica, to measure basal melt in this dynamic region where uncertainties on melt rate estimates are high. We developed a method that accounts for basal geometry complexities and derived a melt rate estimate of ∼22 m per year, which is lower than previous estimates, but it confirms that the basal melt rate Totten Ice Shelf experiences is unusually high for East Antarctica.

1. Introduction

Accurate knowledge of the rate at which ice shelves melt at their base is essential for quantifying the immediate effect of ocean water properties on ice-shelf thickness, a dynamically important quantity for the ice sheet as a whole. When perturbed from a steady state, for example, by a change in ice-shelf thickness due to a change in basal melt rates, an ice sheet will adjust its flow and grounding line position until a new equilibrium is reached. Several ice modeling studies have shown that the Antarctic Ice Sheet is particularly sensitive to thickness changes near grounding lines (Arthern & Williams, 2017; Reese et al., 2018), highlighting the importance of basal melt rate observations in these areas.

Spatial maps of basal melt rates derived from satellite altimetry data have recently become available and are constantly improving (Adusumilli et al., 2020; Moholdt et al., 2014; Rignot et al., 2013). However, major shortcomings of these estimates have been low temporal resolution and the need to rely on assumptions about ice-shelf thickness changes from ice and firn dynamics and surface accumulation. A complementary technique for estimating basal melt rate locally makes use of an autonomous phase-sensitive radio-echo sounder, ApRES (Nicholls et al., 2015). The autonomously sampling ApRES provides Lagrangian measurements of the position of internal and basal reflectors, from which vertical strain rate and basal melt rate are derived. The basal melt rate derivation typically assumes a flat ice shelf base. However, this assumption is likely to fail in the proximity of grounding lines of thick and fast flowing glaciers, where large basal slopes and basal crevassing are expected to occur.

Here, we present ApRES observations from one such location on Totten Ice Shelf (TIS), an ice shelf formed by a large and fast flowing glacier that drains a significant portion of the East Antarctic Ice Sheet

(Greenbaum et al., 2015). Satellite-derived estimates indicate that TIS experiences rates of basal melting that are unusually high for East Antarctica (Depoorter et al., 2013; Rignot et al., 2013), which can be explained by observations of warm modified circumpolar deep water accessing the ice shelf cavity (Rintoul et al., 2016). However, melt rates in this region are difficult to measure precisely due to the complex geometry near the grounding zone. Here, we show how the basal geometry complexities need to be considered in order to derive reliable local melt rate estimates from ApRES observations.

2. Data

An ApRES was deployed on the surface of TIS at site TI05 located ∼7 km from the nearest grounding line (Figure 1). The instrument operated between December 2016 and January 2018, sampling at 90-min intervals. The ApRES used a pair of bow-tie antennas with a predicted half-power beamwidth of 115°. This simple, two-antenna configuration did not allow an aperture to be synthesized, and so the data are one-dimensional (Young et al., 2018). Time series of internal reflector vertical displacements were constructed by cross-correlating the complex signal for each pair of consecutive time shots (Stewart, 2018; Vaňková et al., 2020). These time series were used to obtain time-mean vertical velocity of the internal reflectors, which are typically used to estimate the vertical strain rate profile needed for a basal melt rate estimate (Nicholls et al., 2015). The time series were further used to identify tidal fluctuations following Vaňková et al. (2020). Tidal displacements of internal reflectors are used to determine whether tidal vertical strain rate is depth independent as caused by tidal tilting of the ice shelf (Makinson et al., 2012) or whether the site is tidally bending with a tidal vertical strain rate being a linear function of depth (Jenkins et al., 2006). ApRES melt thinning is typically derived by estimating a vertical velocity profile from internal reflections, extrapolating it to the ice base, and subtracting the strain and surface thinning from the total thinning (Nicholls et al., 2015).

Additionally, during January 2019, a single 240-m long seismic sounding was made at the site. The primary objective of the seismic measurement was to obtain information on bathymetry and the line was oriented approximately along flow. The recording was made using a 24 channel Geometrics Geode data logger at 4 kHz sampling rate with 10-m geophone spacing.

3. Results

Profiles of ApRES-derived quantities from TI05 are shown in Figure 2. The return amplitude decays with range until ∼1,560 m where the first strong reflection appears, marking the beginning of an elevated amplitude return extending to ∼2,200-m range (Figure 2a). The shape of the basal return is unlike that of a typical flat ice shelf where a single strong peak would indicate the location of the base, after which the return would be expected to decay monotonically (e.g., Corr et al., 2002). Here, the basal return amplitude first increases, then plateaus. The strongest reflection is located at ∼300 m greater range than the first strong reflection, and only after that does the return amplitude decay. This complex and protracted basal return indicates the presence of multiple off-nadir reflectors, and it is not immediately clear at which range the base is located and what its shape might be.

The quality of the internal reflectors is relatively good in the upper part of the ice column, but past 650 m it quickly decreases with range as indicated by the decrease in the mean coefficient of correlation between subsequent time shots (Figure 2b). Below 1,560 m, the correlation coefficient abruptly increases again, and the onset and duration of the high correlation coincides with that of the elevated amplitude return. The reflectors in the 800–1,560-m range have low correlation, weak return amplitude (down to ∼−100 dB), and vertical velocities centered around 0 m a^{-1} (Figure 2c), which is all consistent with the signal from this portion of the range being in the noise. Consequently, the vertical strain rate profile can only be derived from vertical velocities in a limited portion of the range. Following Jenkins et al. (2006) we show in the supporting information that a quadratic fit to the derived vertical velocities offers a statistically and physically better fit than a simple linear fit (Figure S2). Thus, the vertical strain rate is more likely a linear function of depth, implying that the site is not in hydrostatic balance and that it experiences bending in the long-term behavior. This has significant implications for the melt rate estimate. Beyond ∼1,560 m the vertical velocities become negative, indicating total thinning and therefore basal melting. However, there are substantial

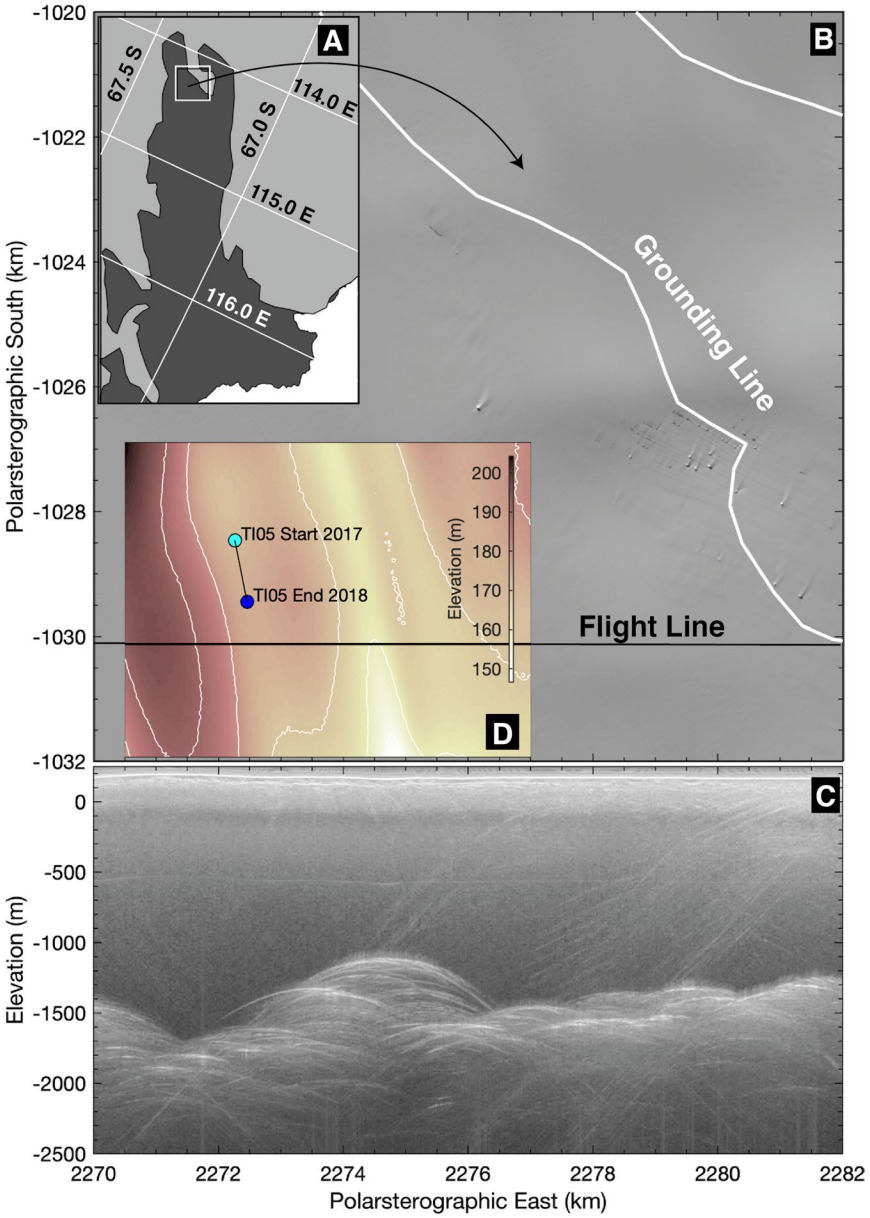

Figure 1. The study area. (a) Totten Glacier Ice Shelf with grounding line from Li et al. (2015). (b) The 2009 airborne radar flight line shown on a Landsat image acquired on December 24, 2018. (c) Airborne radar profile (Blankenship, 2011). (d) REMA surface topography from Howat et al. (2019).

velocity variations with range; tracking the first strong reflection yields a melt rate of just a few m a^{-1} while tracking reflections at a slightly higher range would result in melt rates several times higher. This discrepancy highlights the need to understand the basal geometry at TI05 prior to estimating the basal melt rate.

Finally, the vertical profile of the M_2 tidal amplitude of the vertical displacements, obtained from tidal analysis of vertical displacement time series (Vaňková et al., 2020), shows a striking feature (Figure 2d). The tidal amplitude increases with range until ~600 m where it reaches ~2.5 mm and, while the tidal signal is lost in noise for almost 1,000 m, it reappears again at 1,560 m from where it gradually decreases down to zero by ~1,910–1,950-m range. The two disjointed segments of tidal amplitude appear to follow a single parabola (Figure 2d). The suggested quadratic fit to tidal displacements would be consistent with tidal bending of a ~1,910–1,950-m thick glacier about a neutral surface located approximately half way through the ice column (Jenkins et al., 2006; Vaňková et al., 2020). The phase of the tide (Figure 2e) is the same in both

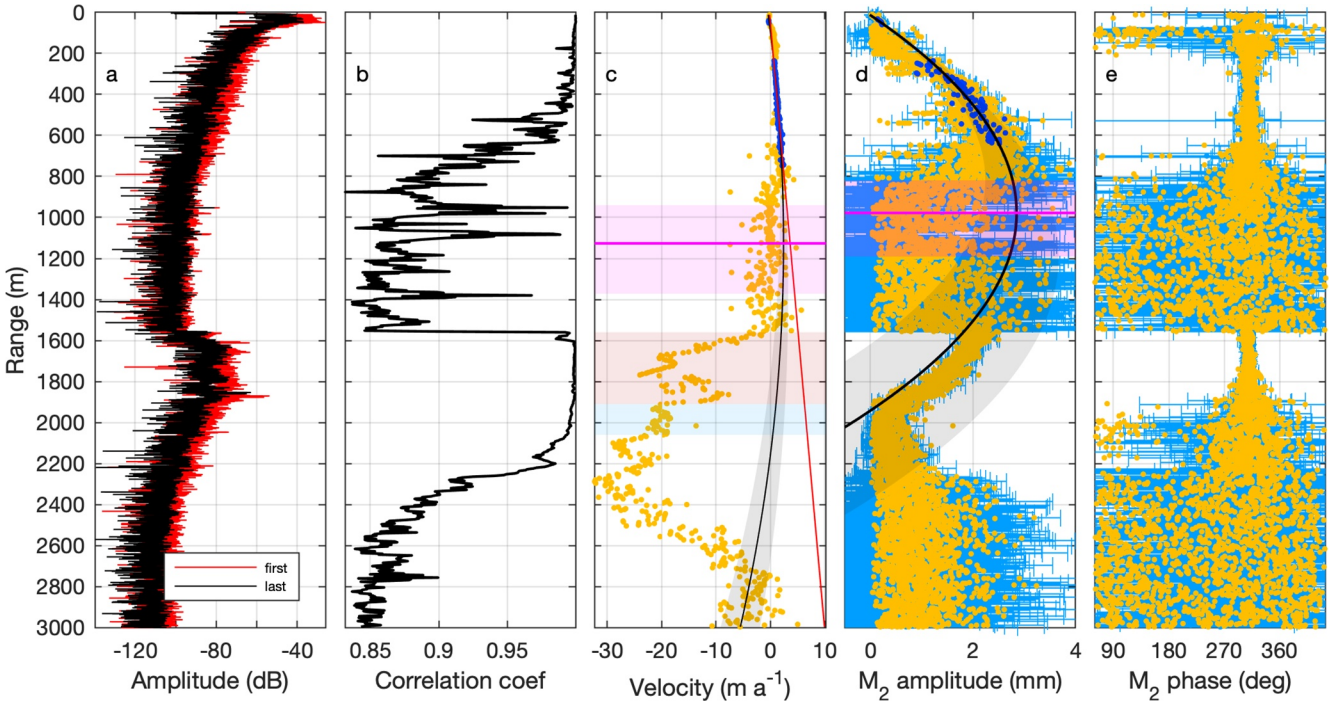

Figure 2. ApRES profiles. (a) Return amplitude from the first and last shots (last shot offset by −5 dB for better visibility). (b) Mean cross-correlation coefficient. (c) Mean velocity (rate of change in range) of internal and basal reflectors. Blue dots mark velocities used to derive the vertical strain thinning at the base by fitting a linear (red) or quadratic (black) function; shading on fits shows standard error. The magenta line shows location of neutral surface for the case of bending and its uncertainty is shaded. The red shaded range corresponds to the inferred face of the basal sloped surface and the blue shaded range to a flat ice base. (d) M_2 tidal amplitude of the line-of-sight displacement with uncertainties marked as blue error bars. Black line is the quadratic fit to the portions of the range marked with blue dots and magenta line the corresponding neutral surface. (e) M_2 tidal phase with uncertainties.

segments of the parabola, indicating that the neutral surface cannot be located closer to the glacier surface than half way through the ice column, otherwise we would observe a phase reversal by 180° at the range equal to twice the neutral depth (e.g., Vaňková et al., 2020).

The seismic record (Figure S1) also gives a complicated return from the base of the ice, with a sequence of arrivals between ∼0.84 s (∼1,560-m depth) and 1.06 s (∼1,950-m depth), implying a number of off-nadir reflections. Relatively high amplitudes imply that the reflections are from an ice-ocean interface and not from internal ice reflectors. This is consistent with an airborne radar profile from 2009, which shows significant basal crevasses in the region (hyperbolic returns in Figure 1c). Additionally, the uppermost reflection in the seismic return (∼0.84 s) does not display the normal move-out that would be expected for a flat surface, indicating that the reflector likely originates from a sloping basal surface, such as the one imaged in the earlier airborne radar profile at 2272.5 km.

4. Discussion

4.1. Melt and Strain From Off-Nadir Reflections

Under the assumption of incompressibility, when ice is deformed in the vertical, a compensating horizontal deformation takes place in order to conserve volume. As a result, when an off-nadir reflector is viewed from the surface during vertical ice deformation, its displacement with respect to the ApRES antennas will have both vertical and horizontal components. This is unlike a reflector at nadir whose displacement will have only a vertical component. The compensating horizontal deformation needs to be taken into account when estimating the strain thinning contribution to the total thinning. Additionally, when vertical strain rate is a function of depth the resulting bending can cause additional line-of-sight (LOS) displacements of these off-nadir reflectors. For a reflector at a known distance from the antennas, the bounds on the strain thinning contribution to the total thinning can be obtained by considering the incompressible case when

deformation takes place along the vertical (z) and one horizontal (x) dimension, that is when $\epsilon_z = -\epsilon_x$ where ϵ is strain along the coordinate indicated by the subscript. Incompressibility is a widely accepted assumption for the case of viscous deformation of ice, and the measurements of Jenkins et al. (2006) showed that this assumption also holds for elastic deformation at tidal time scales. The displacement due to ice deformation (X_o^{strain}) of a reflector initially located at (x_o, z_o) is given by

$$X_o^{strain} = \sqrt{x_o^2 + z_o^2} - \sqrt{\left(x_o(1 + p\epsilon_x) + pdx_c\right)^2 + \left(z_o + \int_0^{z_o} \epsilon_z(z)dz + pdz_c\right)^2}. \quad (1)$$

The dx_c and dz_c terms are displacements due to induced curvature by bending and they are zero for a freely floating ice shelf when the vertical strain ϵ_z is depth independent (depicted in Figure S3). The orientation of the horizontal deformation with respect to the off-nadir reflector is a priori unknown; therefore, we introduce the parameter p and consider two limiting cases in the melt rate estimation. When the horizontal deformation is aligned with the horizontal projection of the line connecting the reflector and the ApRES, $p = 1$, and when the horizontal deformation is orthogonal to the line, $p = 0$ as the there is no horizontal strain rate compensation. The calculation further assumes that ϵ_z does not vary horizontally over the footprint of the radar. If the ice shelf is bending as a thin beam, then $\epsilon_z = \frac{z - H_N}{R}$, where H_N is the neutral surface depth and R is the radius of curvature. Furthermore, $dz_c = R\left(1 - \cos\left(\frac{|\cos(x)|}{R}\right)\right)$ when R is much greater than the ice thickness H, in which case dx_c is negligible. At an ice shelf we always expect $R \gg H$. More complicated vertical strain rate profiles are possible but not considered here.

The time-averaged change in thickness due to melt orthogonal to the basal surface for a reflector located at (x_o, z_o) is given by

$$X_o^{melt} = \frac{X_o^{total} - X_o^{strain} - X_o^{surf}}{\cos\alpha_o}, \quad (2)$$

where X_o^{total} is taken from observations of the mean vertical velocities (Figure 2c), and X_o^{surf} is the mean thickness change due to surface processes and is given by the surface intercept of the fit to the vertical velocities of internal reflectors in Figure 2c. Equation 2 is valid when the melt rate is much smaller than the ice thickness, which is always the case. The $\cos\alpha_o$ factor is a correction that takes into account that the thickness change due to melt for a reflector at (x_o, z_o) is viewed at an angle α_o from nadir (see sketch in Figure S3).

From Equation 1 and 2, it is clear that knowledge of the shape of the basal reflector is essential in order to apply accurate off-nadir corrections to the melt rate estimate via $\cos\alpha_o$ and X_o^{strain}. Once the basal reflector has been identified, the time-averaged basal melt rate estimate ($\dot{m}_e$) over a time interval dt is given by the average over all basal reflectors:

$$\dot{m}_e = -\frac{1}{n_b}\sum_i^{n_b} \frac{X_i^{melt}}{dt}, \quad (3)$$

where n_b is the number of basal reflectors used in the averaging and the negative sign ensures a convention where positive values of $\dot{m}_e$ correspond to melting and negative ones to freezing.

4.2. Basal Geometry From Tides

At TI05, both ApRES and seismic reflections below 1,560 m are strong, implying that they originate from an ice-ocean boundary. However, both data sets also suggest that the first few hundreds of meters of reflections from the ice-ocean boundary may lie off-nadir. These observations imply the presence of a sloped basal surface, potentially originating from a deep basal crevasse or basal channel. The radargram obtained in 2009 (Figure 1c) indicates that deep basal crevassing in this area is likely. Further, the REMA surface topography data set (Howat et al., 2019) suggests that TI05 lies near a basal channel that is several km wide (Figure 1d), providing a potential source of basal slope as well as an explanation for both the long-term and the tidal

bending of the ice column in line with the modeling by Vaughan et al. (2012). We now use the observed tidal information from Figure 2d to test whether a flat ice shelf with a deep basal crevasse or channel could explain the observed vertical velocity profile.

We consider an idealized ice column and prescribe tidal bending via a tidal vertical strain rate varying linearly with depth (Jenkins et al., 2006). The dimensions of the ice column, the extent of bending, and the location of the neutral surface were prescribed to match the best quadratic fit to the observations in Figure 2d. We then calculate the total LOS displacement field as a sum of displacements due to strain and displacements due to the induced curvature of the ice base (Figure S4). Next we prescribe a number of simple basal reflecting surfaces, requiring that the first reflection occurs at 1,560-m range from the ApRES antenna, and observe the LOS displacements from along these reflecting surfaces (Figure 3a). We find that for a flat basal reflecting surface at 1,560 m (Figure 3b) the tidal amplitude does not have the same curvature as observed in Figure 2d and this persists for a flat ice base with a constant slope (Figure 3c). However, the observed curvature can be reproduced by the introduction of a piece-wise linear reflecting surface consisting of a flat base at greater depth and a steep basal slope reaching with its tip up to 1,560-m range (Figure 3d). Further, the LOS tidal displacement amplitude from the steeply sloped surface closely follows the displacement of internal reflections at nadir that would occur on a flat, thicker ice shelf.

The location and slope of the steep basal reflecting surface are poorly constrained by the limited, one-dimensional ApRES data, because the displacements due to strain and the induced curvature partly compensate each other (Figure S4). As a result, the tidal displacement from the steep basal reflecting surface is similar for a wide range of slopes and locations (Figure 3e and 3f). In contrast, we are able to estimate the range to the ice shelf bottom by identifying the distinct transition from quadratic trend in M2 tidal amplitude associated dipping slopes to the relatively linear trend associated with a flat ice bottom (Figure 3d and 3f). For TI05, this change in curvature occurs between ~1,910 and 1,950 m. In this range, the tidal amplitude flattens and appears to increase slowly, which is likely a result of increasing noise in the already low tidal amplitudes; evidence of increasing noise is visible by the elevated uncertainty in the tidal phase with increasing range (Figure 2e). Although the standard error on the quadratic fit results in large uncertainties, because the relatively few points available for fitting are all concentrated in the top third of the ice column, the true neutral surface must lie close to the one from the best quadratic fit, otherwise the tidal displacements at depth could not be reproduced (Figure 3f).

Although the tidal displacements in the 1,560–1,950-m range are consistent with those that would be produced by internal reflectors at nadir, if that were the case, the respective long-term velocities (Figure 2c) would result in an unrealistically complicated vertical strain rate profile for an ice column that is afloat. It is therefore unlikely that we are observing englacial features, such as englacial debris or marine ice. The latter would produce a strong reflection at the marine-meteoric ice interface and weak reflections at greater depths, and result in a scenario similar to Figure 3b. Further, marine ice is saline and therefore highly absorptive and it is unlikely that the signal would penetrate its ~400-m thick layer. Finally, there is no evidence of strongly reflective internal layers on the 2009 radargram (Figure 1c).

The exceptionally good fit of the tidal displacements in the 1,560–1,950-m range to the quadratic displacement curve derived from points in the upper ~650 m, suggest that despite being in a regime where the regular elastic beam model results are not guaranteed to hold because of the irregular basal geometry, the disruptions to the strain field resulting from the irregular geometry are relatively small.

4.3. Basal Melt Rate

The time-averaged basal melt rate at the flat portion of the TI05 ice base is derived using Equation 2. Figure 4b shows how the different terms from Equation 2 contribute to the observed total thickness change at each range bin. The effect of the $\cos\alpha_o$ factor is visualized as an LOS melt correction $X_o^{\alpha_o} = (X_o^{total} - X_o^{strain} - X_o^{surf}) - X_o^{melt}$. As concluded from the analysis of the tidal deformation, the ice shelf base starts at 1,910–1,950-m range and the subsequent returns are assumed to be off-nadir reflections from the flat base. However, as no individual reflector stands out compared with the earlier strong returns (Figure 2a), we use multiple reflections from the flat base to derive an area-averaged melt rate using Equation 3,

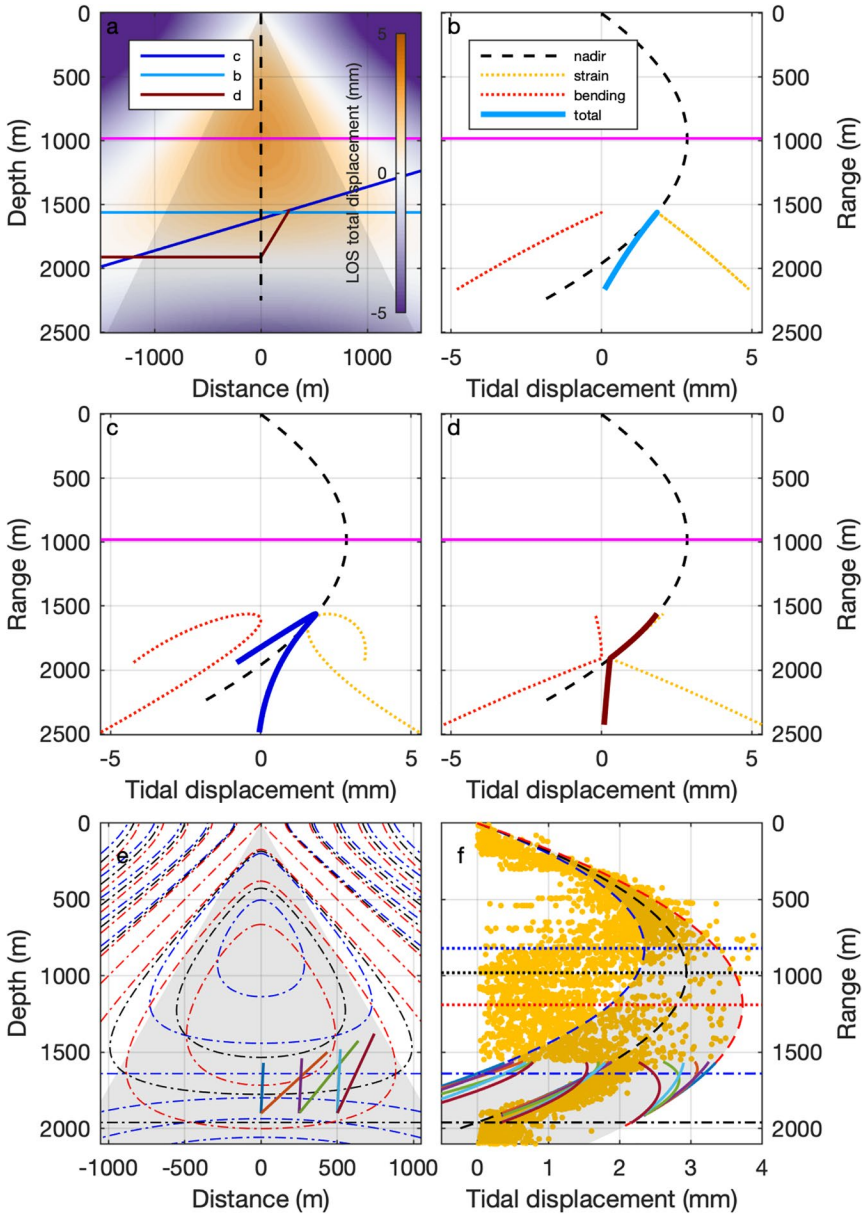

Figure 3. Line-of-sight (LOS) tidal displacement amplitude for various reflecting surfaces upon imposed tidal bending around a neutral surface (magenta line). (a) The total LOS tidal displacement field is shown in the background (see derivation in Figure S4). Different basal geometries are plotted as labeled solid lines and the nadir direction along which internal reflections occur until the range of the first basal reflection is the dashed black line. The shading marks an approximate cone of view of the ApRES located at the axis origin. (b–d) Tidal displacement amplitude along the line-of-sight for each basal geometry in a shown in the respective color. The total displacement of an off-nadir reflecting surface (bold line) is the sum of its displacements due to strain (yellow dotted) and due to bending (orange dotted). The displacement of internal reflectors at nadir is shown for reference (dashed black). Negative displacement would correspond to a phase change by 180° in Figure 2e. (e) Contours of total LOS tidal displacement field for different quadratic fits (color corresponds to respective parabolas in panel f). Basal reflecting surfaces of various slopes are shown in bold lines. (f) Observed tidal displacements as in Figure 2d with different quadratic fits within the standard error. Dashed lines are displacements of internal reflections; dotted, the respective neutral surface; and dash-dotted, twice the neutral surface range. Colored lines show tidal displacements of sloped surfaces in panel (e).

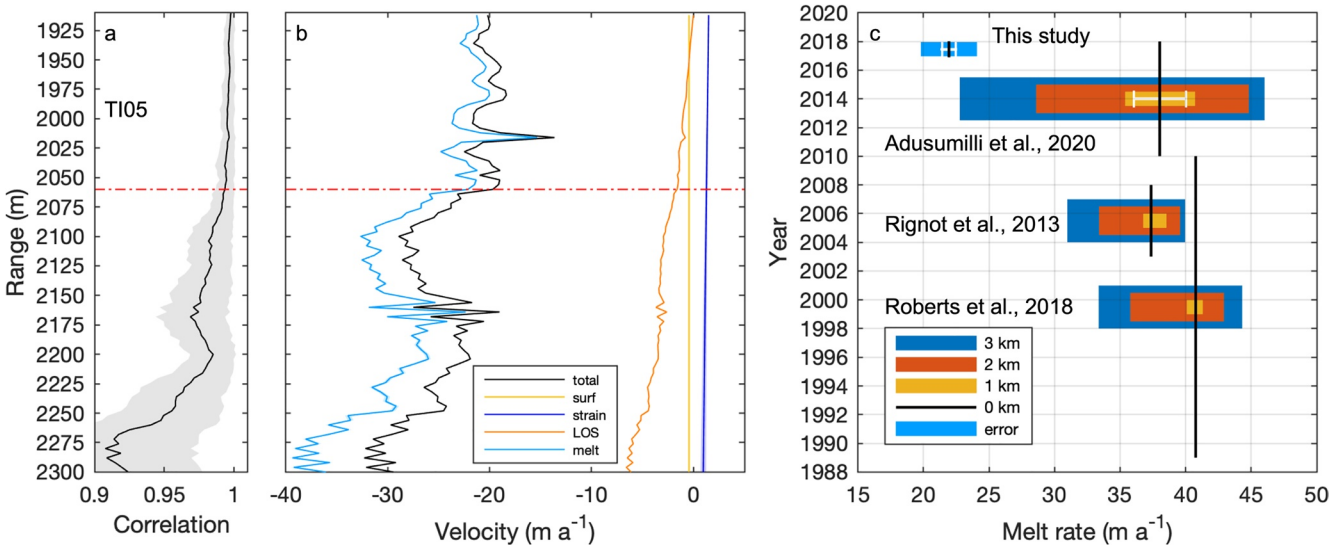

Figure 4. TI05 basal melt rate. (a) Mean cross-correlation coefficient with 1 std dev. shaded. The red line marks range past which the signal becomes weak. (b) Different terms contributing to the observed time-averaged total thinning rate at the ice base. (c) Comparison of ApRES-derived melt rate to existing satellite estimates. The black line shows melt rate interpolated to the mean TI05 location and its vertical extent marks the averaging period for each estimate. For the satellite estimates, the horizontal extent of each rectangle shows the spread of melt rate values within a given distance of the mean TI05 location. White error bars are shown whenever errors were reported. The 99% confidence level on ApRES melt rate associated with averaging over the radar footprint (1,910–2,060-m range above red line in [b]) is marked with white error bars, the horizontal extent of the blue square shows the error associated with extrapolation of vertical strain rate to the ice base, and that is the dominant error term.

once we have corrected for geometry and ice strain. We include reflections located up to 2,060-m range, and so the footprint over which we average has radius of ~700 m. Beyond a range of 2,060 m the correlation coefficient begins to decreases and its standard deviation increases (Figure 4a). Further, the mean melt rate at these further ranges systematically deviates from that in the 1,910–2,060-m range. A similar behavior is observed at the Filchner-Ronne Ice Shelf (FRIS) at sites where the ice base is expected to be flat (Figure S5). Reflectors at greater ranges seem no longer suitable for basal melt rate estimation. In the 1,910–2,060-m range, the melt rate is approximately constant and although there are substantial variations around the mean, there is no range dependence, consistent with the expectation of lack of horizontal gradient in basal melt rate at the spatial scale of a few hundred meters.

Our final TI05 basal melt rate estimate is 22 ± 2.1 m a^{-1} (Figure 4c). The 2.1 m a^{-1} uncertainty consists primarily of uncertainty in the vertical strain rate contribution to total thickness change, which is caused by the limited number of internal reflectors available for the fitting of the strain rate model. The uncertainty in mean melt rate estimated from the melt rate distribution for a fixed vertical strain rate is 0.5 m a^{-1} for a 99% confidence level (Figure 4c). The mean basal melt rate estimate is not significantly affected by the assumption of 1,910-m versus 1,950-m depth of the ice base. Furthermore, the assumption of a flat ice base can be relaxed; at TI05, the effect of the underlying basal slope on the melt rate derivation is small for a basal slope of a few degrees.

The geometry of the steeply sloped basal reflecting surface reaching up to 1,560-m range is poorly constrained and consequently we cannot obtain a reliable basal melt rate estimate for this interface. There are many possibilities for the shape of the basal reflecting surface consistent with the simple bending model (Figure 3f). These include a basal crevasse, a smooth or terraced channel wall, or a combination of both. To derive a melt rate on the basal side wall would require more extensive imaging of the site and possibly a multiple input multiple output ApRES system. The long-term vertical velocities derived from reflectors in the 1,560–1,950-m range (Figure 2c) show abrupt variations with range, although they all indicate that the steep basal surface is melting. These abrupt variations could be interpreted as inhomogeneities on the steep basal slope, and these could in turn result in spatially heterogeneous melt rates at scales of tens to hundreds of meters as previously observed at ice shelf channel walls by Dutrieux et al. (2014).

5. Implications

The ApRES-derived basal melt rate of 22 ± 2.1 m a^{-1} confirms high rates of melting at the back of the TIS cavity and is broadly consistent with the known access available to warm ocean waters (Rintoul et al., 2016), and the great depth of the ice-ocean interface, which increases melting of the ice through reduction of the pressure melting point. Although our melt rate estimate at TI05 is high for East Antarctica, it is significantly lower than existing satellite estimates from this location as shown in Figure 4c. The three available satellite products for the region (Adusumilli et al., 2020; Rignot et al., 2013; Roberts et al., 2018) have somewhat different spatial melt rate pattern (Figures S6a–S6c), but the melt rates near TI05 are well above 30 m a^{-1} (Figures S6d–S6f). We consider melt rates at all grid points that lie within 1-, 2-, and 3-km distance from the TI05 center location and in Figure 4c plot the range of melt rates for each satellite estimate. The ApRES estimate is at least 40% lower than melt rates from within 1-km distance for all satellite estimates and it remains at least 32% lower than melt rates from within 3-km distance for two of the estimates (Rignot et al., 2013; Roberts et al., 2018). The estimate of Adusumilli et al. (2020) has both higher spatial resolution and higher spatial variability, although the latter may be a result of relatively high spatial smoothing in both Rignot et al. (2013) and Roberts et al. (2018). As a result, there are a few points located 3 km east of TI05 whose melt rate estimate lies within the uncertainty of the ApRES measurement.

Part of the discrepancy between the in situ ApRES derivations and the satellite estimates may come from the ice dynamics; while we observe evidence of long-term bending all three satellite estimates assume the ice shelf to be freely floating. Still, assuming depth independent vertical strain rate for the ApRES data and using a linear fit to vertical velocities to extrapolate ice dynamics at the ice base would produce melt rate of only 27 ± 0.6 m a^{-1}, well below the satellite estimates. It remains unclear how representative the TI05 location is of the melt rates in the region and whether the relatively short, year-long period we observed was in any way anomalous. However, our findings highlight the need for independent melt rate estimates that use complementary techniques and instrumentation.

The complexities we have found in the TI05 ApRES data are expected to be common near grounding lines of many ice shelves. This includes basal crevassing causing early off-nadir reflections, relatively thick ice resulting in large uncertainties in the ApRES-derived vertical strain rate and therefore melt rate estimates, and nonconstant vertical strain rates as the ice adjust toward floatation where spatial thickness gradients persist. An effective approach for obtaining in situ melt rates should include predeployment survey to minimize complexities in the basal geometry over the ApRES footprint. In more complex areas, such at TIS, it would also be useful to deploy multiple instruments spaced 1–2 km apart and thus address the question of the true spatial melt rate heterogeneity in the area.

In our analysis, we have shown that even when interested in a long-term mean basal melt rate estimate using ApRES, it can be important to collect a segment of measurements at high temporal frequency, as the tidal dynamics of the ice can be used to constrain the depth of the basal reflector at sites with complex geometries, profoundly affecting the accuracy of the melt rate estimate. Finally, when the basal return is obscured by early off-nadir reflections, using multiple reflections from the ice base to derive basal melt can provide a more robust estimate that is averaged over the footprint of the radar.

The approach presented here will be useful for deriving melt rates in grounding zones of ice shelves, where basal slopes are steep and the density of basal crevasses high. While melt rate derivation at such locations is challenging, these estimates are essential for constraining ice-ocean dynamics in the grounding zone, a major source of uncertainty on ice sheet evolution.

Acknowledgments
This project received grant funding from the Australian Government as part of the Antarctic Science Collaboration Initiative program and the Australian Research Council's Special Research Initiative for Antarctic Gateway Partnership (Project ID SR140300001). Field activities were supported through the Australian Antarctic Science Program grant number 4287. I. Vaňková has received funding from the European Union's Horizon 2020 research and innovation programme under the Marie Skłodowska-Curie grant agreement 790062. We thank two anonymous reviewers for their detailed review which significantly improved the paper.

Data Availability Statement

TI05 ApRES data are available at https://doi.org/10.6084/m9.figshare.12662720.v1. Landsat imagery used in Figure 1 can be obtained from the USGS (https://earthexplorer.usgs.gov) data center.

References

Adusumilli, S., Fricker, H. A., Medley, B., Padman, L., & Siegfried, M. R. (2020). Interannual variations in meltwater input to the Southern Ocean from Antarctic ice shelves. *Nature Geoscience*, *13*, 616–620. https://doi.org/10.1038/s41561-020-0616-z

Arthern, R. J., & Williams, C. R. (2017). The sensitivity of West Antarctica to the submarine melting feedback. *Geophysical Research Letters*, *44*, 2352–2359. https://doi.org/10.1002/2017GL072514

Blankenship, D. D. (2011). *IceBridge HiCARS 1 L0 raw return energy amplitudes,*Version 1. Boulder, CO: NASA National Snow and Ice Data Center. https://doi.org/10.5067/A4XUG9INARYN

Corr, H. F., Jenkins, A., Nicholls, K. W., & Doake, C. S. M. (2002). Precise measurement of changes in ice-shelf thickness by phase-sensitive radar to determine basal melt rates. *Geophysical Research Letters*, *29*(8), 1232. https://doi.org/10.1029/2001GL014618

Depoorter, M. A., Bamber, J. L., Griggs, J. A., Lenaerts, J. T. M., Ligtenberg, S. R. M., van den Broeke, M. R., & Moholdt, G. (2013). Calving fluxes and basal melt rates of Antarctic ice shelves. *Nature*, *502*(7469), 89–92. https://doi.org/10.1038/nature12567

Dutrieux, P., Stewart, C., Jenkins, A., Nicholls, K. W., Corr, H. F. J., Rignot, E., & Steffen, K. (2014). Basal terraces on melting ice shelves. *Geophysical Research Letters*, *41*, 5506–5513. https://doi.org/10.1002/2014GL060618

Greenbaum, J. S., Blankenship, D. D., Young, D. A., Richter, T. G., Roberts, J. L., Aitken, A. R. A., et al. (2015). Ocean access to a cavity beneath Totten Glacier in East Antarctica. *Nature Geoscience*, *8*(4), 294–298. https://doi.org/10.1038/ngeo2388

Howat, I. M., Porter, C., Smith, B. E., Noh, M.-J., & Morin, P. (2019). The reference elevation model of Antarctica. *The Cryosphere*, *13*(2), 665–674. https://doi.org/10.5194/tc-13-665-2019

Jenkins, A., Corr, H. F. J., Nicholls, K. W., Stewart, C. L., & Doake, C. S. M. (2006). Interactions between ice and ocean observed with phase-sensitive radar near an Antarctic ice-shelf grounding line. *Journal of Glaciology*, *52*(178), 325–346. https://doi.org/10.3189/172756506781828502

Li, X., Rignot, E., Morlighem, M., Mouginot, J., & Scheuchl, B. (2015). Grounding line retreat of Totten Glacier, East Antarctica, 1996 to 2013. *Geophysical Research Letters*, *42*, 8049–8056. https://doi.org/10.1002/2015GL065701

Makinson, K., King, M. A., Nicholls, K. W., & Gudmundsson, G. H. (2012). Diurnal and semidiurnal tide-induced lateral movement of Ronne Ice Shelf, Antarctica. *Geophysical Research Letters*, *39*, L10501. https://doi.org/10.1029/2012GL051636

Moholdt, G., Padman, L., & Fricker, H. A. (2014). Basal mass budget of Ross and Filchner-Ronne ice shelves, Antarctica, derived from Lagrangian analysis of ICESat altimetry. *Journal of Geophysical Research: Earth Surface*, *119*, 2361–2380. https://doi.org/10.1002/2014JF003171

Nicholls, K. W., Corr, H. F., Stewart, C. L., Lok, L. B., Brennan, P. V., & Vaughan, D. G. (2015). A ground-based radar for measuring vertical strain rates and time-varying basal melt rates in ice sheets and shelves. *Journal of Glaciology*, *61*(230), 1079–1087. https://doi.org/10.3189/2015JoG15J073

Reese, R., Gudmundsson, G. H., Levermann, A., & Winkelmann, R. (2018). The far reach of ice-shelf thinning in Antarctica. *Nature Climate Change*, *8*(1), 53. https://doi.org/10.1038/s41558-017-0020-x

Rignot, E., Jacobs, S., Mouginot, J., & Scheuchl, B. (2013). Ice-shelf melting around Antarctica. *Science*, *341*(6143), 266–270. https://doi.org/10.1126/science.1235798

Rintoul, S. R., Silvano, A., Pena-Molino, B., van Wijk, E., Rosenberg, M., Greenbaum, J. S., & Blankenship, D. D. (2016). Ocean heat drives rapid basal melt of the Totten Ice Shelf. *Science Advances*, *2*(12), e1601610. https://doi.org/10.1126/sciadv.1601610

Roberts, J., Galton-Fenzi, B. K., Paolo, F. S., Donnelly, C., Gwyther, D. E., Padman, L., et al. (2018). Ocean forced variability of Totten Glacier mass loss. *Geological Society, London, Special Publications*,*461*(1), 175–186. https://doi.org/10.1144/SP461.6

Stewart, C. L. (2018). *Ice-ocean interactions beneath the north-western Ross ice shelf, Antarctica (Thesis)*. Cambridge, UK: University of Cambridge. https://doi.org/10.17863/CAM.21483

Vaňková, I., Nicholls, K. W., Corr, H. F. J., Makinson, K., & Brennan, P. V. (2020). Observations of tidal melt and vertical strain at the Filchner-Ronne Ice Shelf, Antarctica. *Journal of Geophysical Research: Earth Surface*, *125*, e2019JF005280. https://doi.org/10.1029/2019JF005280

Vaughan, D. G., Corr, H. F. J., Bindschadler, R. A., Dutrieux, P., Gudmundsson, G. H., Jenkins, A., et al. (2012). Subglacial melt channels and fracture in the floating part of Pine Island Glacier, Antarctica. *Journal of Geophysical Research*, *117*, F03012. https://doi.org/10.1029/2012JF002360

Young, T. J., Schroeder, D. M., Christoffersen, P., Lok, L. B., Nicholls, K. W., Brennan, P. V., et al. (2018). Resolving the internal and basal geometry of ice masses using imaging phase-sensitive radar. *Journal of Glaciology*, *64*(246), 649–660. https://doi.org/10.1017/jog.2018.54

References From the Supporting Information

Gillet-Chaulet, F., Hindmarsh, R. C. A., Corr, H. F. J., King, E. C., & Jenkins, A. (2011). In-situ quantification of ice rheology and direct measurement of the Raymond effect at Summit, Greenland using a phase-sensitive radar. *Geophysical Research Letters*, *38*, L24503. https://doi.org/10.1029/2011GL049843

Nicholls, K. W. (2018). The study of ice shelf-ocean interaction—Techniques and recent results. *Advances in Polar Science*, *29*(3), 222–230.